The Variable Seismic Signatures of Upwellings in the Transition Zone and Mid-mantle beneath Africa

NERC SCIENCE OF THE ENVIRONMENT

DI31B-0004

UNIVERSITY OF CAMBRIDGE

[1]Alistair Boyce, [1]Sanne Cottaar, [1]Jennifer Jenkins and [1]Stephen Pugh

1 Overview

• **The African superplume, is widely considered to have caused the ~30Ma volcanism at the Ethiopian traps. The contribution of more localised upwellings to African volcanism, that may or may not originate below the mantle transition zone is the subject of considerable debate.**

• **Thermochemical conditions impart control on the depth at which mantle materials undergo phases changes, causing impedance contrasts. Observations of seismic discontinuities from the mantle transition zone (MTZ) and below can therefore provide insight into the variable thermochemical nature of upwellings beneath Africa.**

• **Here we present observations of seismic discontinuities beneath Africa obtained from a compilation of P-to-s (Pds, PPds, and PKPds) receiver functions derived from publicly available seismograph networks across Africa from 1990-2019.**

• **We capitalise on a new high-resolution P-wave absolute velocity model for the African continent (Boyce et al., in prep.) to migrate our receiver functions to depth prior to common conversion point (CCP) stacking.**

• **We interrogate our receiver function CCP stacks for MTZ discontinuity topography at a range of frequencies and for discontinuities at mid-mantle depths (~1000km) to understand better the variable thermochemical nature of mantle upwellings that have contributed to recent volcanism across Africa.**

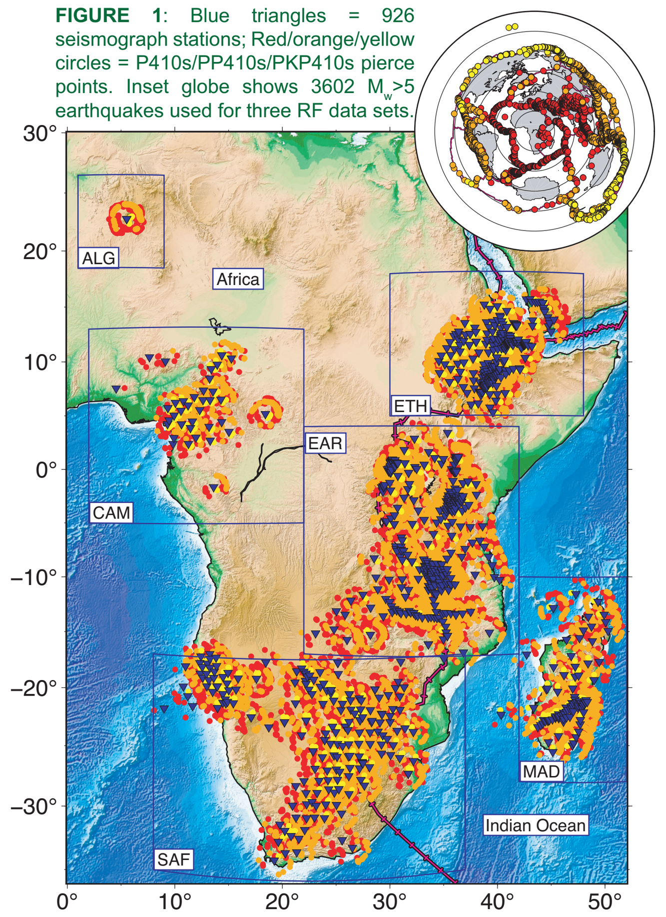

FIGURE 1: Blue triangles = 926 seismograph stations; Red/orange/yellow circles = P410s/PP410s/PKP410s pierce points. Inset globe shows 3602 M_w>5 earthquakes used for three RF data sets.

2 Receiver function calculation

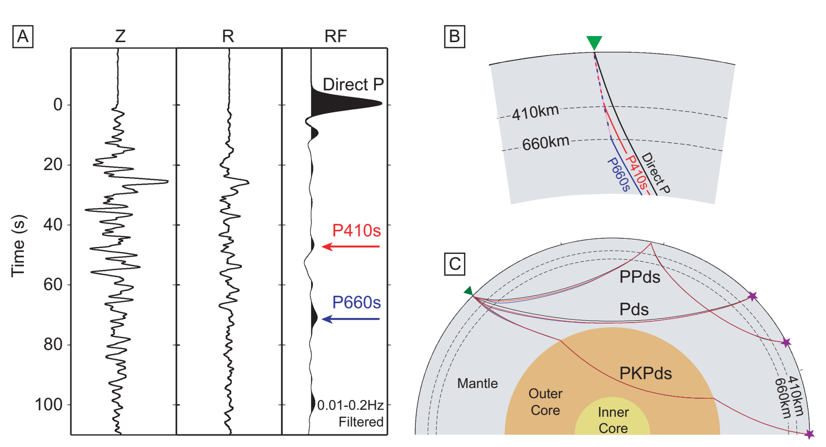

FIGURE 2 (ABOVE): (A) Example vertical component seismogram (Z) deconvolved from radial component (R) to produce Pds phase receiver function (RF). Low amplitude P-to-s converted phases from top and bottom of the MTZ are indicated. (B) Ray path diagram showing incoming converted P (solid) to s (dashed) phases at MTZ discontinuities w.r.t. direct P phase. (C) Converted and direct phases take largely similar paths throughout Earth's mantle. Adapted after Jenkins et al., (2016).

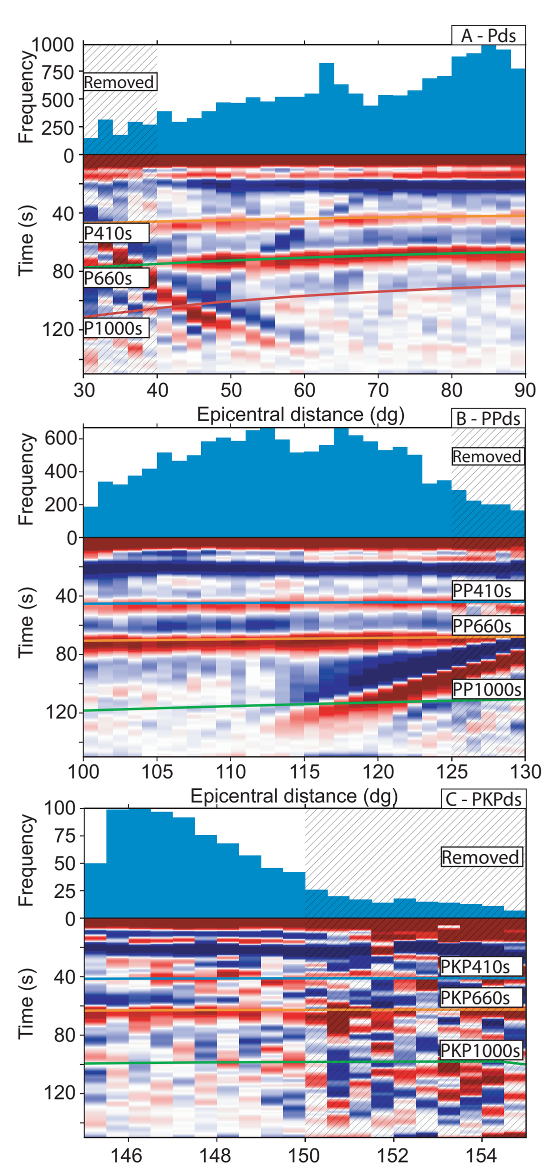

FIGURE 3 (RIGHT): Receiver functions (filtered at 0.01-0.2Hz) binned by epicentral distance for ~16,000 Pds RFs (A), ~13,000 PPds RFs (B) and ~900 PKPds RFs (C). Predicted moveout of converted phases are labelled. "Removed" epicentral distance bins are excluded from subsequent CCP stacking to limit interference of multiples with converted arrivals from MTZ.

• Waveform data set sourced from publicly available stations across Africa (1990-2019) through IRIS, GEOFON and RESIF data centres.

• Receiver functions (RFs) are calculated using time-domain iterative deconvolution (Ligorría and Ammon,1999) initially built with 5s width Gaussian pulses to obtain a representation of earth structure along incoming ray paths (Figure 2).

• Pds, PPds, PKPds phases recorded at 30-90°, 100-130°, 145-155° epicentral distance respectively (Figure 3A-C).

• We impose epicentral distance restrictions upon these data to avoid phase interference (Figure 3) and apply strict automated QC (after Cottaar and Deuss, 2016).

3 Depth conversion and CCP stacking

• Delay times of S-phases can be converted to a discontinuity depth using an upper mantle velocity model.

• To account for the spread of conversion points (Figure 1) and the increasing Fresnel zone width with depth (Figure 4), we use weighted common conversion point (CCP) stacking (e.g., Cottaar and Deuss, 2016).

• RF amplitudes are back propagated along ray paths and stacked using a radially decreasing weighting at grid points within 2 Fresnel zone half widths (Figure 4).

• Initially we compute discontinuity depths using ak135 (Kennett et al., 1995 - Panel 4).

• Subsequently we use an upper mantle shear wave model - SL2013SV (Schaeffer and Lebedev, 2013) and a new V_P model for Africa - BBAFRP20 (Boyce et al., in prep. - Panel 5).

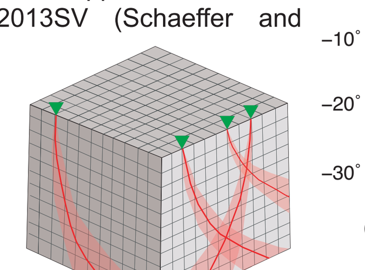

FIGURE 4: Schematic of receiver function common conversion point stacking.

FIGURE 5: Stacking weights at 410km and 660km depth in CCP volumes combining epicentral distance restricted Pds, PPds and PKPds data sets (Figure 3).

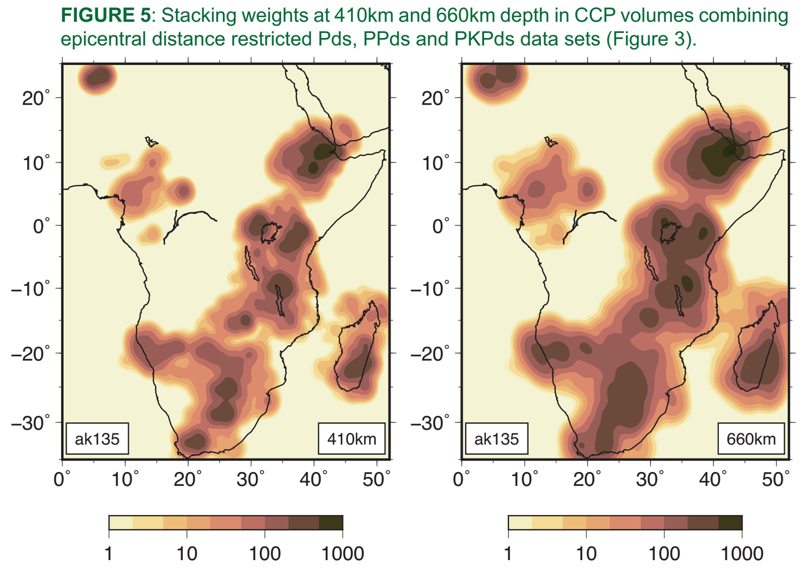

4 CCP stack 1D velocity model - ak135

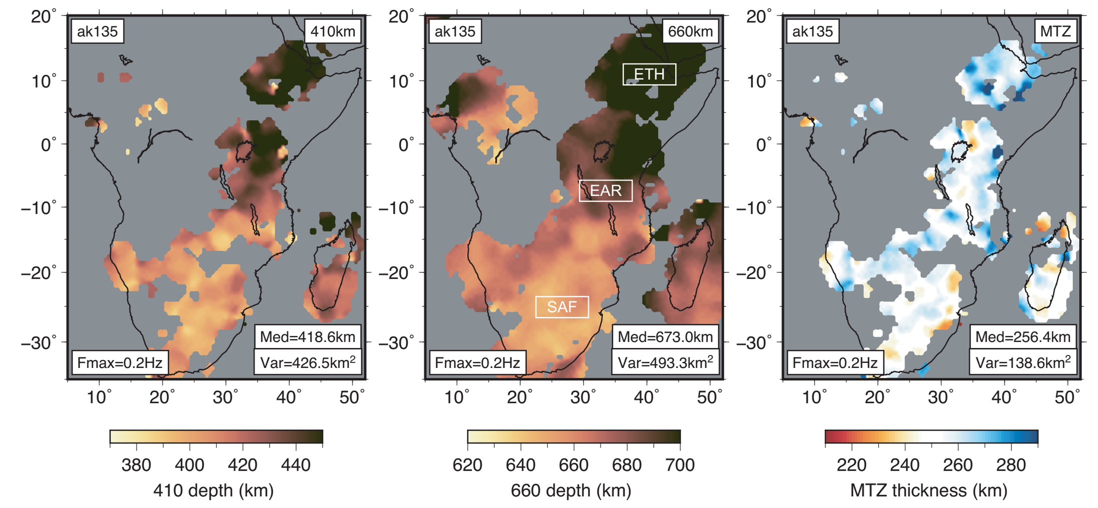

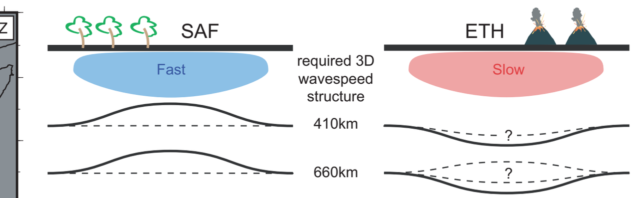

FIGURE 6 (LEFT): MTZ discontinuity depths/thickness using ak135 depth conversion for regions in which weight and standard error in CCP amplitude is > 2.

FIGURE 7 (ABOVE): Schematic of velocity model depth correction effect on expected MTZ discontinuity depths. Solid lines = observed, dashed = expected discontinuities.

FIGURE 8 (BELOW): SW-NE waveform cross-section through ak135 CCP volume. Yellow ticks = depths of maximum amplitudes above 2 standard error for MTZ discontinuities..

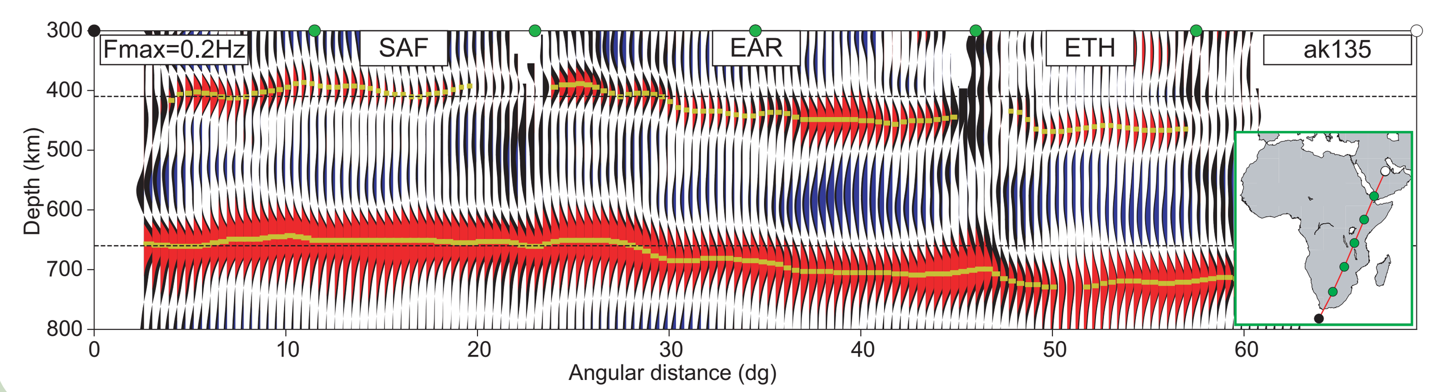

• Correlation of topography on 410km and 660km discontinuity implies upper mantle 3D velocity variations are significant.

• We use two 3D tomographic velocity models to better-correct discontinuity depths (Panels 5-8).

5 3D mantle velocity structure

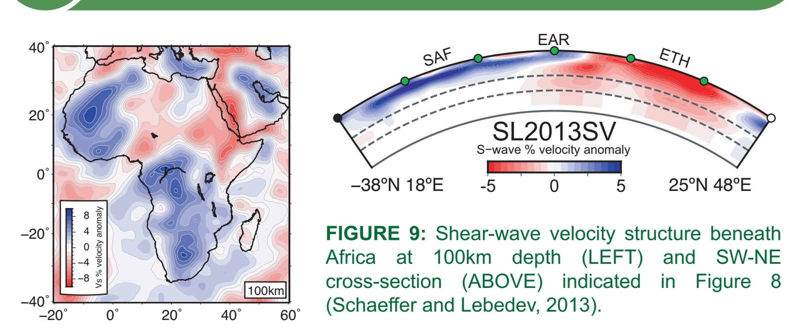

FIGURE 9: Shear-wave velocity structure beneath Africa at 100km depth (LEFT) and SW-NE cross-section (ABOVE) indicated in Figure 8 (Schaeffer and Lebedev, 2013).

• Continental CCP stacks computed using depth corrections from SL2013SV and a new V_P model BBAFRP20 (Figures 9, 10).

• Global P-phase pick database (1964-2007), inverted for absolute V_P structure using an adaptively parameterized, LSQR inversion scheme (Li et. al., 2008).

• Supplemented with >87,000 absolute P-wave delay times from African temporary networks (1990-2019) calculated using AARM (Boyce et al., 2017).

• Upper mantle V_P structure of southern and eastern Africa well resolved beneath available stations (Figure 1).

• Slow V_P anomaly extends from CMB below southern Africa across MTZ below EAR. Evidence for additional sub-vertical slow V_P anomaly below Ethiopia/Somalia.

• Velocity anomalies are anticorrelated between V_S and V_P (SL2013SV and BBAFRP20) in upper mantle below EAR.

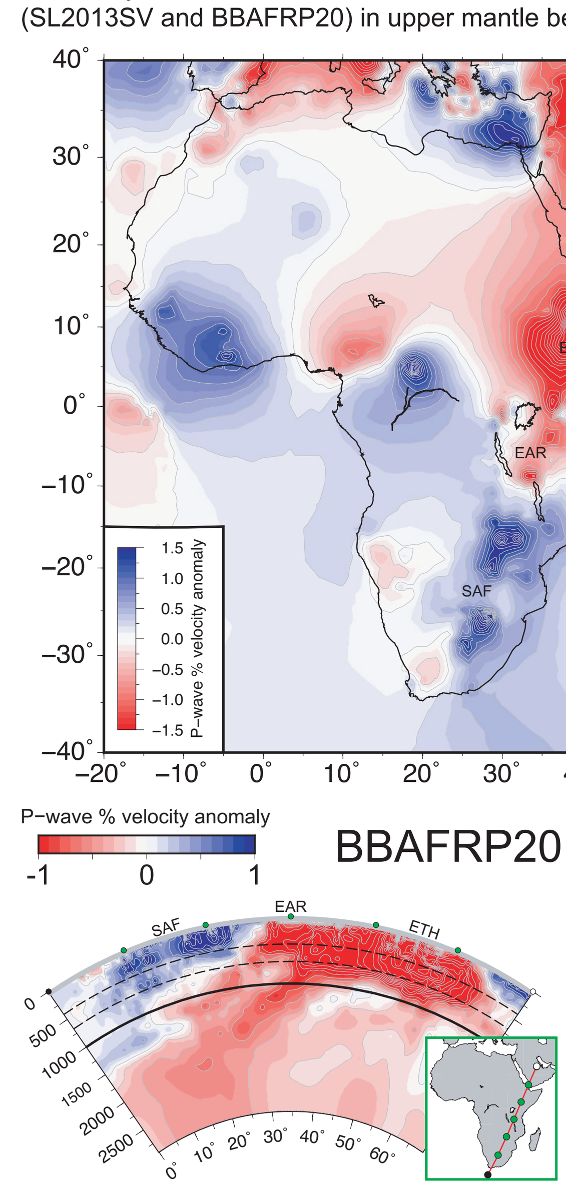

FIGURE 10 (ABOVE): Absolute V_P structure for BBAFRP20 at 100km depth, plotted as deviation from ak135 (dVp %). Grey contours plot 0.2% velocity anomaly deviations where colour scale saturates. (LEFT): SW-NE cross section through African superplume in BBAFRP20. (Boyce et al., in prep).

6 CCP stack 3D velocity models - SL2013SV & BBAFRP20

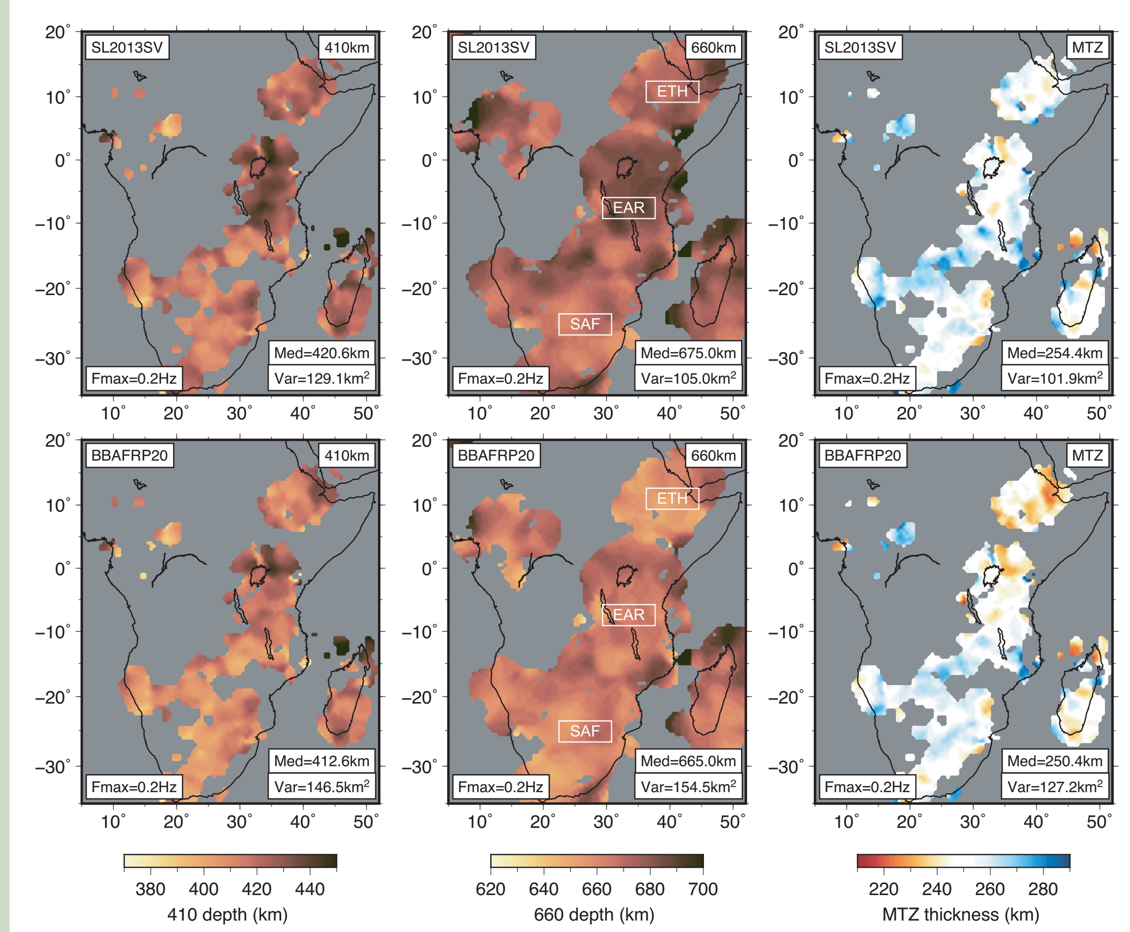

FIGURE 11 (ABOVE): MTZ discontinuity depths/thickness using SL2013SV and BBAFRP20 depth conversion for regions in which weight and standard error in CCP amplitude is > 2.

FIGURE 12 (RIGHT): Interpretation guide for MTZ discontinuity depths for a warm upper mantle. Opposing clapeyron slopes of ringwoodite and majorite phase transitions to perovskite can produce 660km discontinuity topography.

FIGURE 13 (BELOW): SW-NE waveform cross-section through SL2013SV (TOP) and BBAFRP20 (BOTTOM) CCP volumes. Yellow ticks = depths of maximum amplitudes above 2 standard error for MTZ discontinuities.

• Removal of 410/660km correlation using 3D velocity models.

• No significant discontinuity topography beneath SAF (southern Africa).

• 410km discontinuity not visible in Cameroon, potential evidence for water filled MTZ (Buchen et al., 2018)?

• Depressed 660km beneath EAR, evidence for uplifted 660km beneath ETH (BBAFRP20).

• Linear Vp-Vs anomaly scaling in depth corrections may cause EAR MTZ topography differences (Figures 9, 10)?

• EAR: Depressed 410&660km = Garnet?

• ETH: Depressed 410km, uplifted 660km (BBAFRP20) = Olivine?

• Evidence for variable response of 660km to thermochemical conditions beneath EAR-ETH.

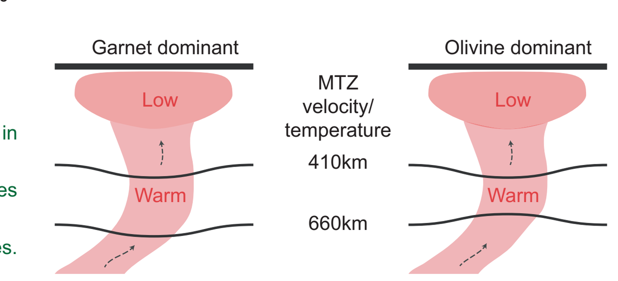

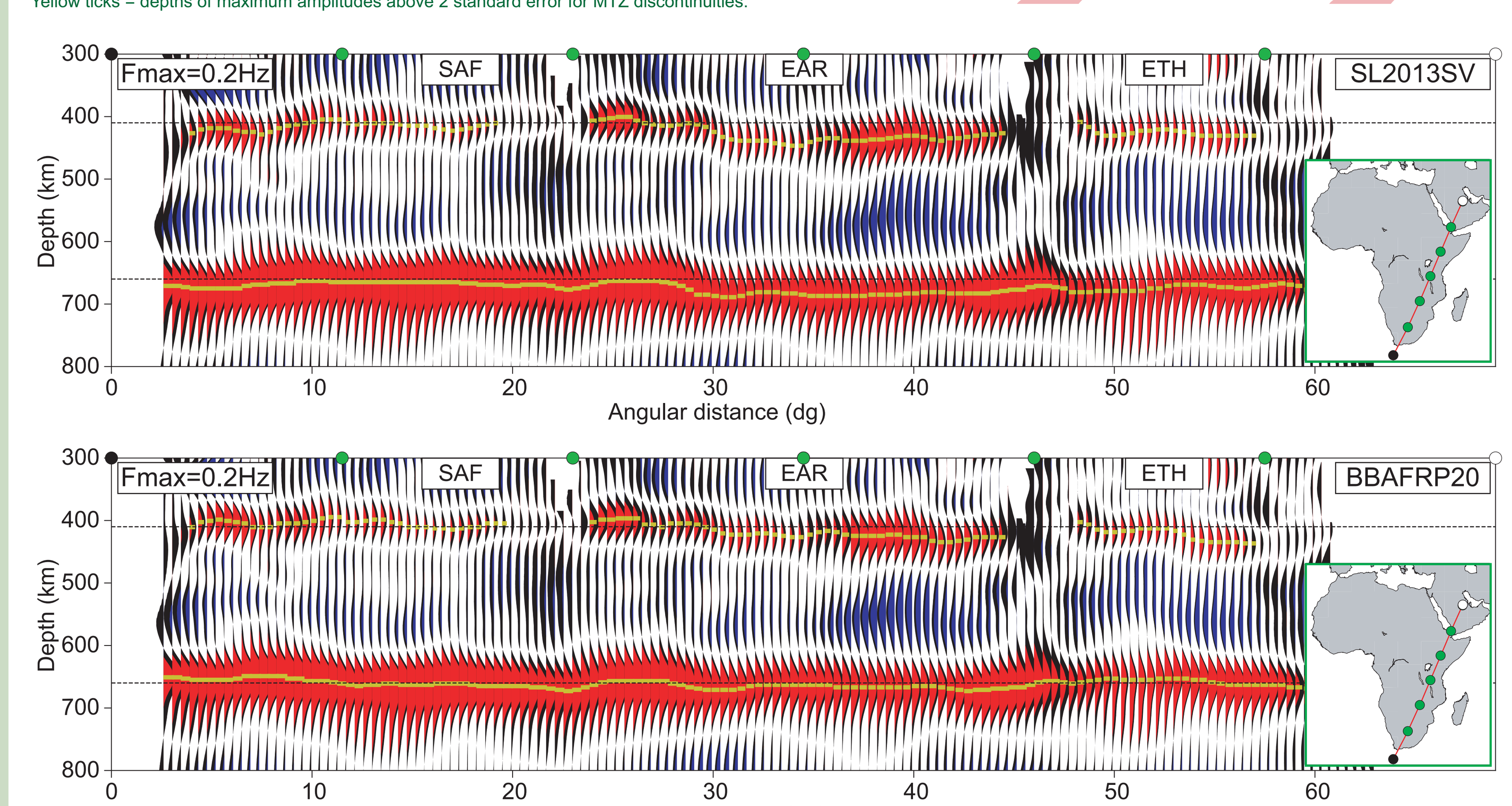

7 Mid-mantle observations

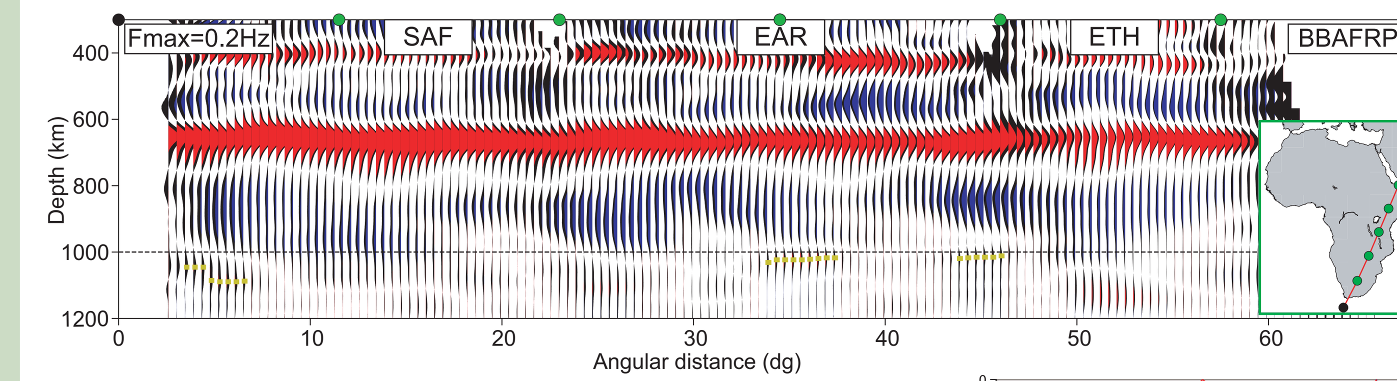

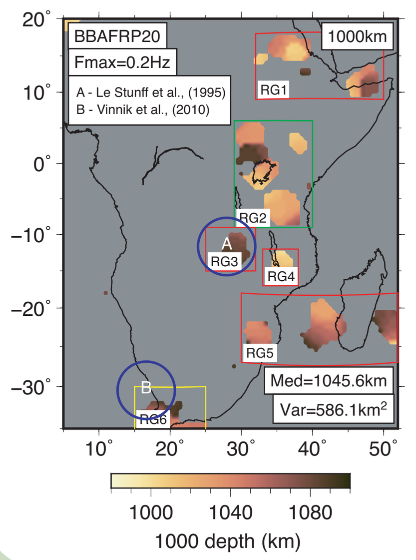

FIGURE 14 (ABOVE): SW-NE cross-section through BBAFRP20 CCP volume to 1200km depth. Yellow ticks = depths of maximum amplitude above 2 standard error in 980-1100km depth range.

FIGURE 15 (LEFT): Mid-mantle discontinuity depth map grouped by region in which weight and standard error in CCP amplitude is > 2. Region bounding box colour represents confidence in discontinuity based on slowness stack multiple/conversion assessment (green - high, red, low). Previous mid-mantle discontinuity observations are highlighted in blue circles.

FIGURE 16 (RIGHT-TOP): Ray path diagram highlighting shallow/steep incidence angle of a surface multiple/converted arrivals compared to direct-P phase. (RIGHT-BOTTOM): Slowness stack for Pds data with 1000km depth pierce-points within RG2 - high confidence result - green arrow. Predicted converted Pds arrivals have negative slowness (solid line), multiples have positive slowness (dashed line) w.r.t. direct-P phase.

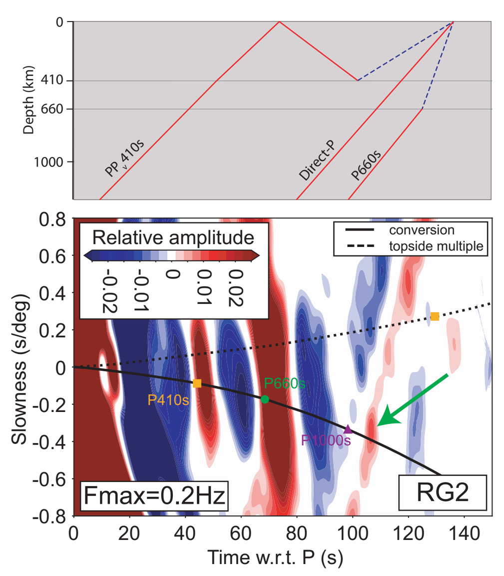

• Observations of Pds conversions beneath EAR (Figure 14 and RG2 - Figure 15) at ~1025km depth.

• Slowness assessment (Figure 16) highlights coherent arrival for observations in RG2 (green arrow), lower confidence in mid-mantle conversions elsewhere.

• Converted arrival from ~1025km depth in RG2 collocated with slow wavespeeds in BBAFRP20 at 1000km depth - green arrow (Figure 17).

• A warm MTZ displaying depressed 410km and 660km discontinuities, underlain by a ~1000km depth discontinuity may indicate entrained heterogeneity in a plume.

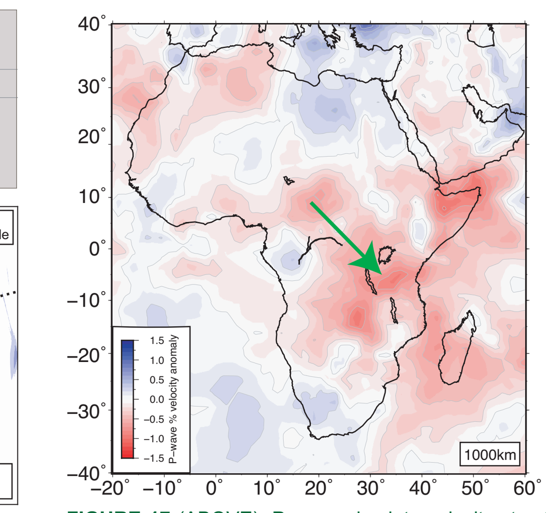

• Chemically distinct plume material may derive from recycled basaltic material or a deep sourced LLSVP reservoir (Jenkins et al., 2017).

FIGURE 17 (ABOVE): P-wave absolute velocity structure for BBAFRP20 (Boyce et al., in prep) at 1000km depth, plotted as deviation (dVp %) from ak135.

8 Frequency analysis

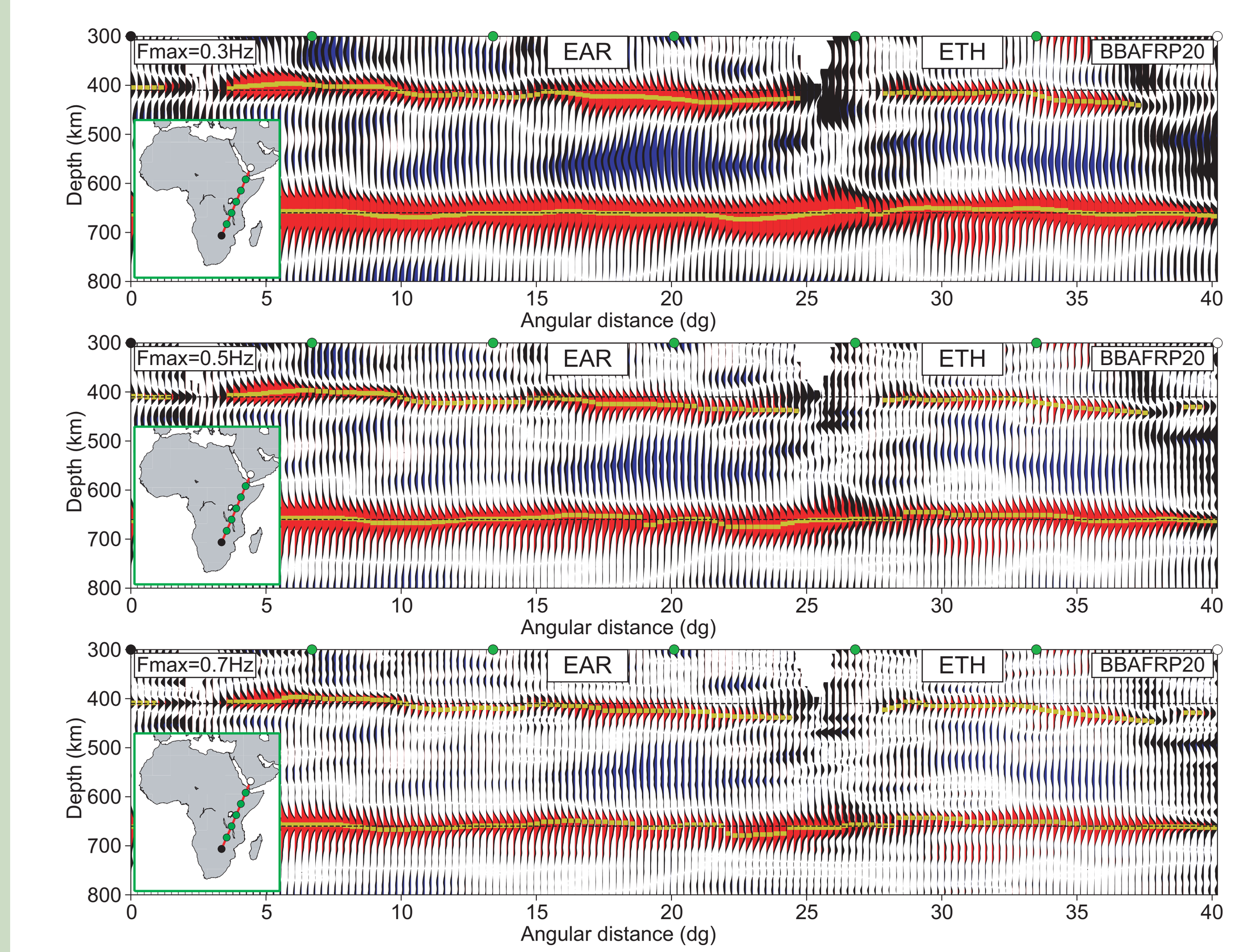

FIGURE 18: SW-NE waveform cross-section through BBAFRP20 CCP volumes using RFs of increasing maximum frequency (Fmax=0.3-0.7Hz). Yellow ticks = depths of maximum amplitudes above 2 standard error for MTZ discontinuities.

• 660km discontinuity depth is uplifted across three frequency bands beneath ETH.

• 660km discont. appears shallower at high frequencies below EAR, evidence for two peaks/mineral phase transitions between ~650-700km depth.

• Presence of both ringwoodite and majorite phase transitions to perovskite below EAR?

9 Key points

• BBAFRP20 P-wave tomographic model provides appropriate time-to-depth correction for RF stacks across Africa.

• Coherent 410km not visible in Cameroon, water in the MTZ?

• Variable character of warm MTZ beneath east Africa; a variable source in depth or deep mantle reservoir(?):

- **EAR:** Frequency dependent, Garnet(?) dominant MTZ, 1000km discont.

- **ETH:** Olivine(?) dominant MTZ, no 1000km discont.

• Support for variable source of volcanism in east Africa - two plumes?

Hypothesis: The African superplume samples chemically distinct material from LLSVP whilst a vertical plume beneath Ethiopia/Afar does not?

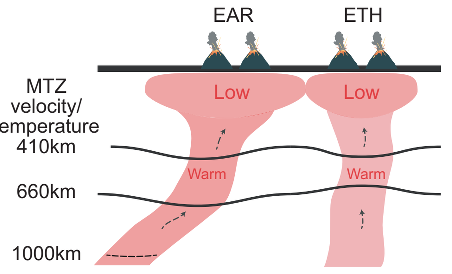

FIGURE 19: Schematic interpretation of variable character of mantle upwellings beneath east Africa.

References
Boyce, A., et al., (2017), From relative to absolute teleseismic travel-times: the Absolute Arrival-time Recovery Method (AARM), *Bull. Seis. Soc. Am.*, **107(5)**, 2511–2520.
Boyce, A., et al., (in prep), Insights into the extent of mantle upwellings and cratonic keel modification beneath Africa from absolute arrival-time P-wave tomography.
Buchen, J. et al., (2018), High-pressure single-crystal elasticity of wadsleyite and the seismic signature of water in the shallow transition zone, Earth Planet. Sci. Lett. 498, pp.77-87.
Cottaar, S. and Deuss, A., (2016). Large-scale mantle discontinuity topography beneath Europe: Signature of akimotoite in subducting slabs. J. Geophys. Res., **121(1)**, pp.279-292.
Jenkins, J., et al., (2016), Depressed mantle discontinuities beneath Iceland: Evidence of a garnet controlled 660 km discontinuity?. Earth Planet. Sci. Lett., **433**, pp.159-168.
Jenkins, J., et al., (2017), Converted phases from sharp 1000 km depth mid-mantle heterogeneity beneath Western Europe. Earth Planet. Sci. Lett., 459, pp.196-207.
Kennett, B.L.N., et al., (1995), Constraints on seismic velocities in the earth from traveltimes. *Geophys. J. Int.*, **122**, 108–124.
LeStunff, Y et al., (1995), P'P' Precursors Under Africa: Evidence for Mid-Mantle Reflectors, Science, **270(5233)**, pp.74-77.
Li, C., et, al., (2008), A new global model for P wave speed variations in Earth's mantle, *Geochem. Geophys. Geosyst.*, **9**, Q05018.
Ligorria, J.P. and Ammon, C.J., (1999), Iterative deconvolution and receiver-function estimation. *Bull. Seis. Soc. Am.*, **89(5)**, pp.1395-1400.
Schaeffer, A.J. and Lebedev, S. (2013), Global shear speed structure of the upper mantle and transition zone, *Geophys. J. Int.*, **194(1)**, 417–449.
Vinnik, L.P. et al., (2010), Mid-mantle layering from SKS receiver functions, Geophys. Res. Lett., **37**, L24302.

ab2568@cam.ac.uk

[1]Department of Earth Sciences, University of Cambridge, Cambridge, UK. *A.B.* is funded by the Natural Environment Research Council Grant number NE/R010862/1 from PI ***S.C.***